J Mater Sci (2009) 44:55–63
DOI 10.1007/s10853-008-3123-y

Characterisation of bauxite and seawater neutralised bauxite residue using XRD and vibrational spectroscopic techniques

Sara J. Palmer · Ray L. Frost

Received: 28 August 2008 / Accepted: 20 November 2008 / Published online: 20 December 2008

Abstract Bauxite refinery residues are derived from the Bayer process by the digestion of crushed bauxite in concentrated caustic at elevated temperatures. Chemically, it comprises, in varying amounts (depending upon the composition of the starting bauxite), oxides of iron and titanium, residual alumina, sodalite, silica, and minor quantities of other metal oxides. Bauxite residues are being neutralised by seawater in recent years to reduce the alkalinity in bauxite residue, through the precipitation of hydrotalcite-like compounds and some other Mg, Ca, and Al hydroxide and carbonate minerals. A combination of X-ray diffraction (XRD) and vibrational spectroscopy techniques, including mid-infrared (IR), Raman, near-infrared (NIR), and UV–Visible, have been used to characterise bauxite residue and seawater neutralised bauxite residue. The ferric (Fe^{3+}) ions within bauxite residue can be identified by their characteristic NIR bands, where ferric ions produce two strong absorption bands at 25,000 and 14,300 cm^{-1}. The presence of adsorbed carbonate and hydroxide anions can be identified at around 5,200 and 7,000 cm^{-1}, respectively, attributed to the 2nd overtone of the 1st fundamental overtones observed in the mid-IR spectra. The complex bands in the Raman and mid-IR spectra around 3,500 cm^{-1} are assigned to the OH-stretching vibrations of the various oxides present in bauxite residue, and water. The combination of carbonate and hydroxyl units and their fundamental overtones give rise to many of the features of the NIR spectra.

S. J. Palmer · R. L. Frost (✉)
Inorganic Materials Research Program, School of Physical and Chemical Sciences, Queensland University of Technology, Brisbane, QLD, Australia
e-mail: r.frost@qut.edu.au

Introduction

Bauxite refinery residues (red mud) are derived from the Bayer process by the digestion of crushed bauxite in concentrated caustic (NaOH) at elevated temperatures [1]. The process results in the dissolution of gibbsite ($Al(OH)_3$) and boehmite as sodium aluminate, while the remaining insoluble residue (45% liquor and 55% solid mud), known widely as red mud (RM), is removed by means of flocculation and decantation [1–3]. Red mud varies in physical, chemical, and mineralogical properties due to differing bauxite ore sources and refining processes employed [4, 5]. The general consensus of the composition of red mud has been found to be largely composed of iron oxides, primarily hematite (Fe_2O_3), and goethite (FeOOH), boehmite (AlOOH), other aluminium hydroxides, calcium oxides, titanium oxides (anatase and rutile), and aluminosilicate minerals (sodalite) [3, 6–8].

The full characterisation of these waste materials needs to be understood to ensure the residue is safely disposed of and that suitable storage facilities are constructed. Bauxite refinery residues are characterised by relatively high concentrations of sodium aluminate and sodium carbonate and a variety of anionic species. If left untreated, these species have the potential to be detrimental to the environment. Therefore, systems have been developed to remove these species prior to disposal. A number of alumina refineries have implemented the neutralisation of red mud with seawater, and found it provided a reduction in both pH and dissolved metal concentrations [5, 8]. Seawater neutralisation results in the neutralisation of alkalinity through the precipitation of Mg, Ca, and Al hydroxide and carbonate minerals, where the formation of hydrotalcite-like compounds assist in the reduction of dissolved metals in the liquor. The carbonate and bicarbonate alkalinity of the

waste is primarily removed through the precipitation of calcite and aragonite [9].

Minerals containing oxidised iron (Fe^{3+}), such as hematite in red mud, have a characteristic red colour. The spectra of Fe^{3+} minerals exhibit electronic transitions localised to the FeO_6 coordination site. Sherman and Waite [10] synthesised several Fe_2O_3 and FeOOH polymorphs (hematite, maghemite, goethite, lepidocrocite) and analysed their spectra in the near-IR to UV region. The report showed that these minerals consisted primarily of Fe^{3+} ligand filed transitions [10]. Characterisation of red mud is made possible by the effect of structural cationic substitutions (Al^{3+}, Fe^{3+}, Ti^{3+}, Ca^{2+}, Fe^{2+}) on band shifts in the high wavenumber region, 40,000–7,500 cm^{-1} and vibrational modes of carbonate ion and OH units in the region 7,300–4,000 cm^{-1}.

The objective of this investigation is to characterise red mud, before and after seawater neutralisation. Determination of any changes in the composition of red mud would assist in the identification of possible reactions that take place during the seawater neutralisation process. The result of the work will be used for further investigations on the mechanism/s involved in the seawater neutralisation process. The UV–Vis–NIR diffuse reflectance spectroscopy (DRS) approach was undertaken to study the cationic distribution in red mud before and after seawater neutralisation.

Experimental

The Queensland Research and Development Centre (QRDC) RioTintoAlcan, provided red mud from a Rio Tinto Alumina refinery. Seawater neutralised red mud (SWN-RM) was prepared by treating red mud with 4.5 times the volume of seawater in a dropwise fashion. Characterisation of red mud and SWN red mud included: X-ray diffraction, Raman spectroscopy, IR spectroscopy, UV–Vis spectroscopy, and near-IR spectroscopy.

X-ray diffraction patterns were collected using a Philips X'pert wide angle X-ray diffractometer, operating in step scan mode, with Co Kα radiation (1.78897 Å). Raman spectra were excited by a HeNe laser (633 nm) at a nominal resolution of 2 cm^{-1} in the range between 100 and 4,000 cm^{-1}, using a Renishaw 1000 Raman BHSM microscope. More detail of the experimental technique is provided in a previous study by the authors [11].

Infrared spectra (over the 4,000–525 cm^{-1} range) were obtained using a Nicolet Nexus 870 FTIR spectrometer with a smart endurance single bounce diamond ATR cell. A Varian Cary 5000 UV-Visible NIR spectrophotometer, equipped with diffuse reflectance accessory (DRA) was employed to record the electronic spectrum of the samples in the region between 200 and 1,100 nm (50,000–9,090 cm^{-1}). NIR spectra were collected on a Nicolet Nexus FT-IR spectrometer with a Nicolet near-IR Fibreport accessory (Madison, Wisconsin). Spectra were obtained from 13,000 to 4,000 cm^{-1} (0.77–2.50 μm) by the co-addition of 128 scans at a spectral resolution of 8 cm^{-1}.

Results and discussion

X-ray diffraction

Due to the complexity of red mud numerous mineralogical phases were identified using XRD. The XRD patterns of RM and SWN red mud are given in Fig. 1, with major peaks labelled. The XRD pattern obtained for red mud (RM) and SWN-RM show that hematite and gibbsite are the major components present. XRD results identified 12 different mineralogical phases present in RM and SWN-RM, table not given, with the exception that SWN-RM showed an additional mineralogical phase, hydrotalcite. These results are in good agreement with literature [12]. The mineralogical complexity of bauxite residues has also been reported by Castaldi et al. [13]. The seawater neutralisation process produces hydrotalcite-like compounds through the neutralisation of free OH^- with Mg, Al, and Ca to form hydroxycarbonates. Other compounds such as boehmite, cancrinite, whewellite, anatase, calcite, and quartz are some of the other phases identified.

The comparison of the XRD patterns of RM and SWN-RM show a slight reduction in the intensity of hematite peaks, and a more significant decrease is observed for gibbsite at 18 $2\theta°$. A decrease in intensity suggests a possible phase transition of gibbsite occurs. The change in intensity suggests that gibbsite is involved in chemical reactions during the seawater neutralisation process. These observations agree with those of Sherman and Waite [10]. This variability in intensity also suggests that the crystallinity or the particle size of gibbsite and hematite is affected by the seawater neutralisation process. A broad peak at approximately 12 $2\theta°$ is characteristic of the $d_{(003)}$ peak for hydrotalcite ($Mg_6Al_2(OH)_{16}(CO_3) \cdot 4H_2O$), [12], which is produced during the seawater neutralisation process. The weak intensity of this peak is due to the overshadowing of the sharper and more crystalline mineralogical phases present. The broadness of the hydrotalcite peak suggests poor crystallinity, due to a short formation period. Hydrotalcites were prepared in the absence of RM (SWN of Bayer liquor) and found that the same broadness of this peak is observed. Other components detected by XRD appear to be unaffected by the seawater neutralisation process.

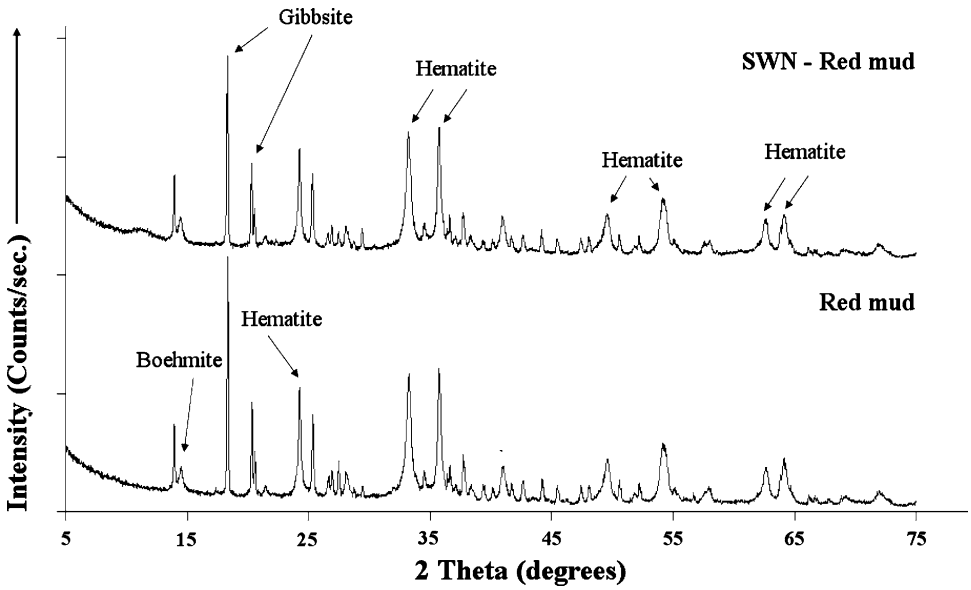

Fig. 1 Comparison of the XRD patterns of RM and SWN-RM

Raman spectroscopy

The Raman spectra for RM and SWN-RM are shown in Fig. 2. The broadness of the bands indicates multiple components are present in the same wavenumber region, and therefore band component analysis is carried out. The rich red colour of red mud is due to iron oxides, in particular hematite. Hematite belongs to the $D3_{6d}$ crystal space group and seven phonon lines are expected in the Raman spectrum, namely two A_{1g} modes (225 and 498 cm^{-1}) and five E_g modes (247, 293, 299, 412, and 613 cm^{-1}) [14]. Peaks assigned to hematite dominate the spectra due to the large quantity of hematite in the samples. Peaks at 223, 246*, 291, 408, 610, 658, and 1,318 cm^{-1} are observed for RM and are in good agreement with values reported [14]. Similar peaks have been observed in SWN-RM at 225, 247*, 292, 408, 613, 660, and 1,324 cm^{-1}. Band positions with * are determined by band component analysis, figures not shown. The peak at 1,320 cm^{-1} has been previously reported by Hart et al. [15], and was assigned to the 2-magnon scattering of hematite.

The very intense peak at around 145 cm^{-1} is ascribed to the O–Ti–O bending vibration associated with anatase. The band at 145 cm^{-1} could belong to either anatase or rutile (both of which are present in red mud), however it was ascribed to anatase as the intensity of the peak is strong, unlike the rutile peak. Five bands are assigned to anatase, the two strongest bands are located at 146 and 638* cm^{-1}, and three weaker bands at around 199*, 397*, and 514* cm^{-1} [16]. The band at 632 and 635 cm^{-1}, RM and

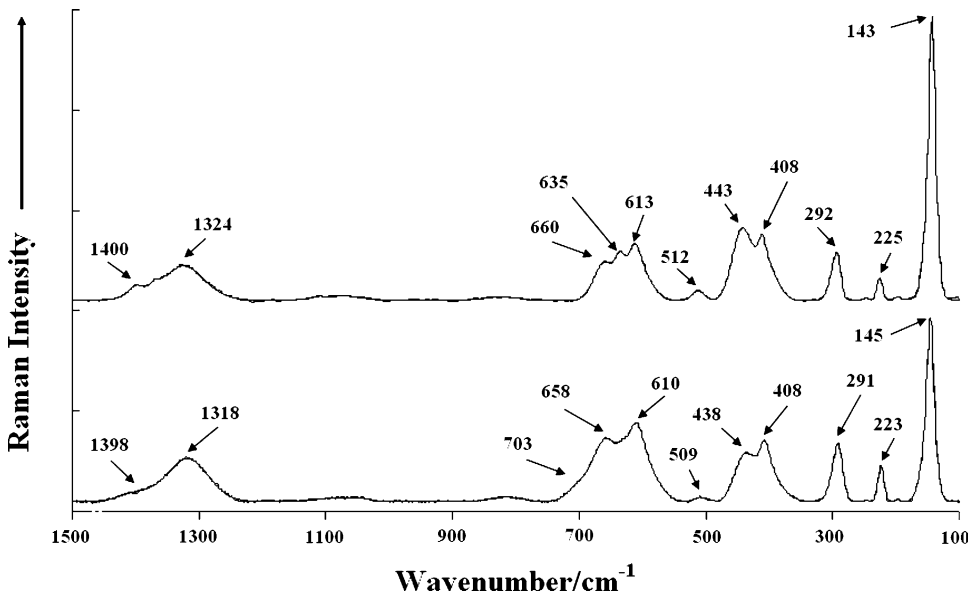

Fig. 2 Raman spectra of red mud (bottom) and seawater neutralised red mud (top)

SWN-RM, respectively, are assigned to the deformation modes of anatase. Analysis of RM and SWN-RM using Raman microscopy is not quantitatively comparable, as only a small spot size (1 μm) is analysed using this technique. Therefore, the increase in intensity of the anatase bands for SWN-RM is due to a larger concentration of anatase being present in the 1 μm area analysed. All bands reported by Murad [16], are observed in this investigation. Bands at around 1,400, 509, 223, and 197 cm^{-1} are believed to be attributed to whewellite ($Ca(C_2O_4) \cdot H_2O$) [17], an organic impurity found in red mud. Other components detected using Raman spectroscopy were gibbsite, boehmite, calcite, and quartz, Table 1.

Cancrinite and sodalite are common sodium aluminosilicate compounds that form in strongly caustic alkaline aqueous solutions. Cancrinite has characteristic Raman band positions at 1,057, 524, 469, and 443 cm^{-1}, where the band at around 1,057 cm^{-1} is attributed to the antisymmetric stretch, ν(Al–O–Si) of the aluminosilicate framework [18]. Bands at lower wavenumbers are attributed to the symmetric stretch of the aluminosilicate framework [18]. The Raman spectra of both red mud and SWN red mud show these characteristic cancrinite band positions; however, slight shifts to lower wavenumbers are observed. These bands are relatively weak in comparison to peaks associated with gibbsite and hematite, thus suggesting that only a small percentage of cancrinite is present in the bulk material. Many of the cancrinite band positions overlap with gibbsite band positions. Therefore, the dramatic increase in the band at around 440 cm^{-1} is believed to be due to an increase in gibbsite. This is supported by all gibbsite bands increasing in intensity in the SWN-RM, unlike bands associated with cancrinite. This is clearly shown for the cancrinite band at 457 cm^{-1}, which is observed for RM but not for SWN-RM.

Infrared spectroscopy

Hydroxyl-stretching region

Water hydroxyl-stretching vibrations are intense in infrared spectroscopy because of the large change in dipole moment. However, water is a very weak Raman scatterer and the ν(OH) modes are not as intense in a Raman spectrum. Due to fluorescence in the Raman spectra no bands were detected in the water hydroxyl-stretching vibrational region. The infrared spectra of the hydroxyl-stretching region of RM and SWN-RM are given in Fig. 3. Both the RM and SWN-RM show a broad, intense band centred at approximately 3,400 cm^{-1}, due to the stretching modes of hydroxyl groups and water molecules in the aluminium, iron, silica, titanium, and calcium oxides. Band component analysis is used to identify the bands present. Both RM and SWN-RM show a complicated spectrum with

Table 1 Raman wavenumbers and relative intensities (*vs* very strong, *s* strong, *m* medium, and *w* weak) for RM and SWN-RM [15, 19, 20, 23]

Red mud samples		Reference wavenumbers							
Red mud	SWN-RM	Hematite	Cancrinite	Whewellite	Gibbsite	Boehmite	Calcite	Anatase	Quartz
1398 (m)	1,400 (m)			1,402					
1318 (s)	1,324 (s)	1,322 (s)							
1084 (w)	1,111 (w)						1,085		1,085
1048 (w)	1,069 (w)		1,057		1,051	1,072			
816 (w)	823 (w)			896	816				811
658 (s)	660 (s)	657 (m)				674			
632 (m)	635 (s)							638 (m)	
610 (s)	613 (s)	610 (m)		601	617				
509 (w)	512 (w)		524	509	506			514 (w)	510
494 (w)		498 (w)				495			
457 (m)			469			451			464
438 (s)	443 (s)		443		444				
408 (s)	408 (s)	412 (s)			412				
398 (m)	386 (m)				396	360		397 (w)	
303 (w)	299 (w)		301		306				
291 (s)	292 (s)	293 (s)	277		290		282		
246 (w)	247 (w)	246 (w)		251	242				
223 (s)	225 (s)	227 (s)		223		228			
145 (vs)	143 (vs)			141				146 (vs)	

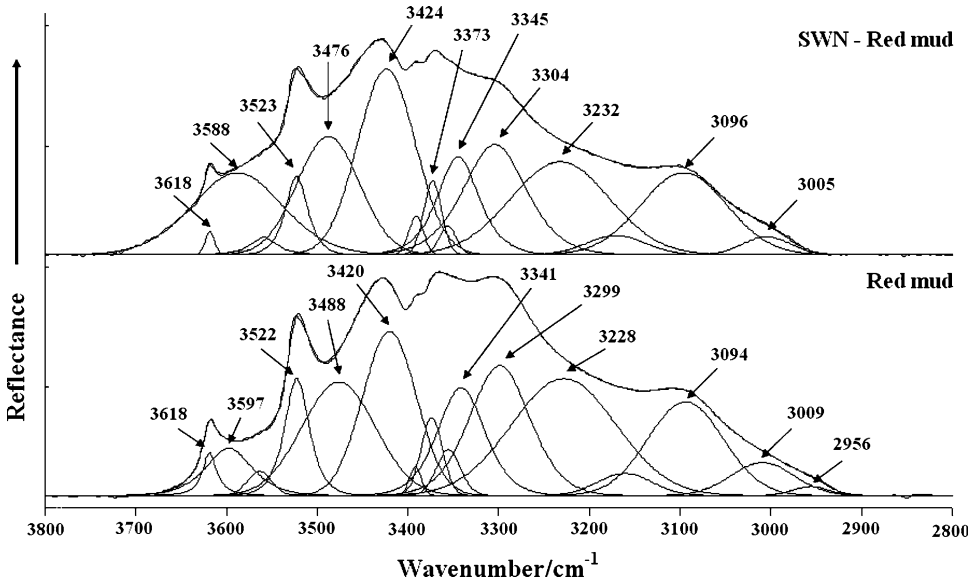

Fig. 3 Infrared spectra of RM and SWN-RM in the 3,800–2,800 cm^{-1}

up to 16 infrared hydroxyl-stretching bands being observed. The assignment of the bands is difficult because of the complex band profile and the overlap of bands.

Infrared absorption bands located at around 3,618, 3,520, 3,428, and 3,380 cm^{-1} are assigned to the ν(OH)-stretching modes of gibbsite [19, 20]. For RM four infrared absorption bands are observed at 3,618, 3,522, 3,420, and 3,374 cm^{-1}, and two infrared emission bands are observed at 3,355 and 3,488 cm^{-1}. For SWN-RM four infrared absorption bands are observed at 3,618, 3,523, 3,424, and 3,373 cm^{-1}, and two infrared emission bands are observed at 3,356 and 3,476 cm^{-1}. The band positions observed are in good agreement with those reported by Frost [20] and Farmer [19]. The intensity of bands at 3,618 and 3,522 cm^{-1} decreases after seawater neutralisation, which agrees with the results found by XRD analysis that a phase transition may occur for gibbsite. The bands assigned to gibbsite appear as the sharper bands in the infrared spectra. The hydroxyl deformation modes of gibbsite were observed at 1,069, 1,030, 964, and 913 cm^{-1} for RM, and for SWN-RM the bands are observed at 1,066, 1,031, 972, and 915 cm^{-1}, data not shown. The broad band at 3,597 and 3,588 cm^{-1}, RM and SWN-RM, respectively, are believed to be due to a combination of OH-stretching vibrations of H_2O bonded to M–OH units (where M might be Mg or Al or any combinational permutation of these metals). The intensity of this band increased significantly after the SWN process. It is therefore proposed that the increase is due to the formation of hydrotalcite and an increase in the number of Mg–OH bonds present in SWN-RM. The increase in broadness of this band is proposed to be due to the overlapping of Mg–OH and Al–OH bands associated with the newly formed hydrotalcite structure. Bands at lower wavenumbers, 3,094 and 3,096 cm^{-1}, for RM and SWN-RM, respectively, are believed to be due to strongly hydrogen bonded H_2O to carbonate. The broadness of the band suggests that there are multiple components contributing to the shape of this band. For RM the infrared absorption bands for boehmite are observed at 3,299, 3,094, and 3,009 cm^{-1}, and for SWN-RM, the infrared absorption bands are located at 3,304, 3,096, and 3,005 cm^{-1} [19, 21].

The surfaces of hematite crystals are covered with hydroxyl groups, and although they are not structural OH groups, the vibrations of which can appear in the infrared spectrum. Rochester and Topham [22] reported 11 such bands the most significant of which were at 3,720 (shoulder), 3,700, 3,635, 3,490 (shoulder), 3,435 (shoulder), and 3,380 cm^{-1}. Even though hematite are detected using XRD and Raman spectroscopy, none of these bands are observed in the IR spectra. It is suggested that surface hydroxyl groups were removed during the drying process; therefore, expected bands are weak and undetectable.

Carbonate vibrations

The infrared spectra of RM and SWN-RM in the region 1,800–1,200 cm^{-1} are highly complex with multiple bands that overlap, shown in Fig. 4. Interpretation of the individual bands is difficult, due to the number of carbonates present in red mud. Carbonates generally show strong infrared absorptions in the region 1,450–1,400 cm^{-1} (ν_3), medium absorption bands between 890 and 800 cm^{-1} (ν_2), and at 760–670 cm^{-1} (ν_4) [23]. Carbonates that are of aragonite-type observe the symmetric stretch (ν_1) at around 1,120–1,040 cm^{-1} [23]. Figure 4 shows a broad band stretching from 1,700 to 1,300 cm^{-1} with multiple bands in the ν_3 region, suggesting that there are several carbonates

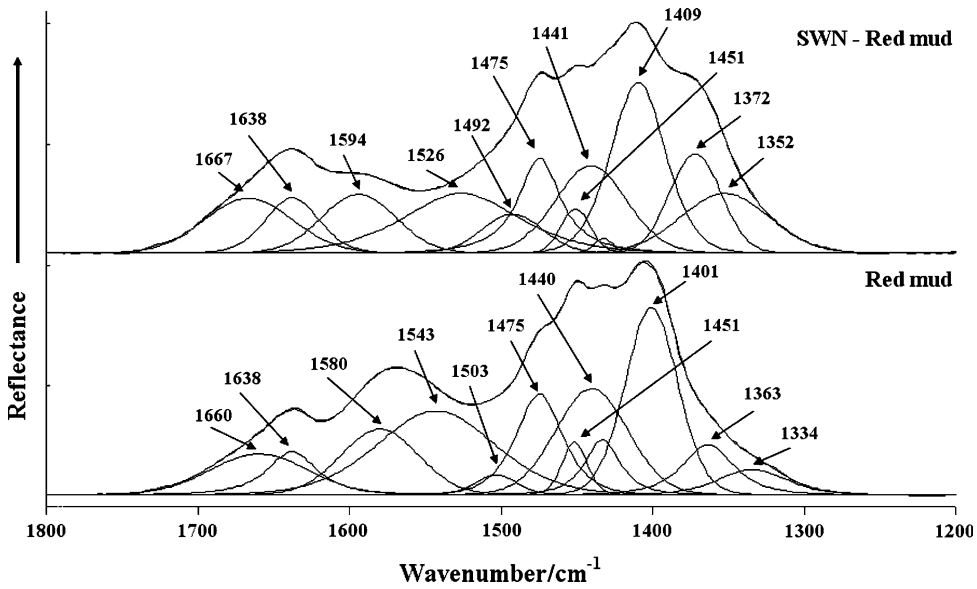

Fig. 4 Infrared spectra of RM and SWN-RM in the 1,800–1,200 cm^{-1}

present in both RM and SWN-RM. Four infrared absorption bands are observed at 1,475, 1,440, 1,451, and 1,401 cm^{-1} for red mud, and at 1,475, 1,441, 1,451, and 1,409 cm^{-1} for SWN red mud. No significant changes in the v_3 band positions are observed. The v_4 and v_2 vibrational modes are observed, however figures are not shown.

Typically red mud contains 2–8 wt% calcite ($CaCO_3$). Five vibrational frequencies are expected for calcite: 1,444, 1,435, 1,099, 876, 724, and 712 cm^{-1} [19]. The infrared spectra of RM and SWN-RM show similar bands as reported by Farmer [19]. Five of the six infrared bands for calcite are observed at 1,440, 1,433, 1,096, 875, and 724 cm^{-1} for red mud. The corresponding bands for calcite for SWN red mud are observed at 1,441, 1,432, 875, and 728 cm^{-1}, lower wavenumber figures are not given. The intensity of the calcite peak at 1,440 and 1,433 cm^{-1} decreased after neutralisation slightly. It is suggested that a slight dissolution of calcite occurred. The intensity of the Raman bands corresponding to calcite vibrations is very weak; however, the fundamental mode is observed at 1,084 and 1,111 cm^{-1}, RM and SWN-RM, respectively. The reason for the weak intensity of the Raman band is believed to be due to the large quantity of hematite and gibbsite minimising the significance of the calcite bands. It is therefore proposed that the detection/identification of small concentrations of calcite in these types of complex samples would be best analysed using infrared spectroscopy.

Cancrinite ($Na_6Ca_{1.5}Al_6Si_6O_{24}(CO_3)_{1.6}$) also exhibits carbonate vibrations at 1,505, 1,480, 1,438, 1,400–1,390 cm^{-1} [19]. Four infrared bands are observed for RM at 1,503, 14,750, 1,440, and 1,401 cm^{-1}, and at 1,492, 1,475, 1,441, and 1,409 cm^{-1} for SWN-RM. Bands at 1,363 and 1,334 cm^{-1}, for RM, and at 1,372 and 1,352 cm^{-1}, for SWN-RM, are characteristic infrared bands of whewellite ($Ca(C_2O_4) \cdot H_2O$). It appears the quantity of whewellite increases after neutralisation, the intensity of 1,363 and 1,334 cm^{-1} bands in SWN-RM increased significantly. The increase in whewellite is believed to be due to the increase in free Ca^{2+} ions introduced through the addition of seawater that then complexes with oxalic acid in solution forming whewellite. Bands at higher wavenumbers, 1,660 and 1,638 cm^{-1} for RM and 1,667 and 1,638 cm^{-1} for SWN-RM, are assigned to the bending modes of strongly hydrogen bonded H_2O. The bands at around 1,660 cm^{-1} are attributed to H_2O bonded to carbonate anions, whilst the bands at around 1,638 cm^{-1} are attributed to H_2O bonded to OH anions. These bands are believed to be due to a combination of vibrations associated with water in different environments. The shift to higher wavenumbers, seen for SWN-RM, at 1,667 cm^{-1} is thought to be due to the formation of hydrotalcite, increasing the strength of the bond. The presence of a band at 1,580 and 1,594 cm^{-1}, RM and SWN-RM, respectively, is proposed to be non-hydrogen bonded H_2O (water vapour).

UV–Vis spectroscopy

The spectra of Fe^{3+} $(O/OH)_6$ group of minerals in the extended UV–Vis region to NIR include two broad bands near 650 nm and 900 nm and one sharp band at 400 nm [10, 24, 25]. The optical absorption spectra in the UV–VIS–NIR (VNIR) of RM and SWN-RM are shown in Fig. 5. The bands are diffuse and weak in intensity due to the Fe^{3+} transitions being spin-forbidden [26]. The individual bands were resolved by the application of component analysis. The broad band centred around 860 nm (11,630 cm^{-1}) with a shoulder near 665 nm

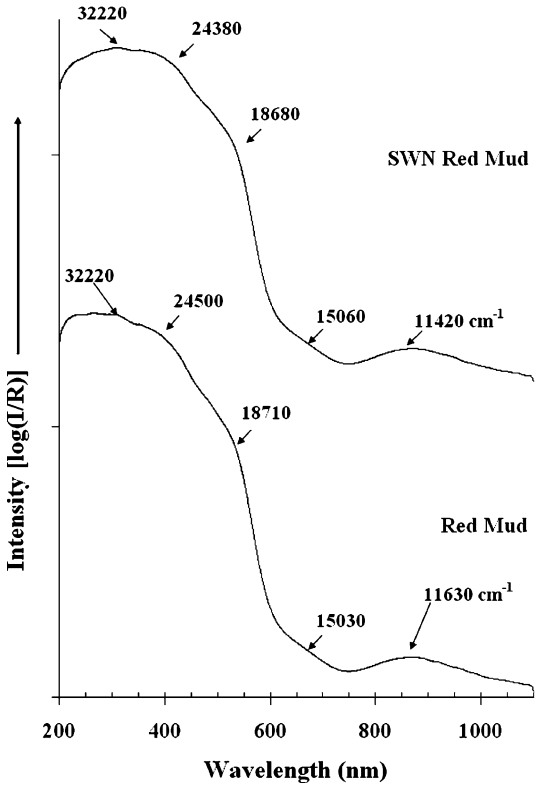

Fig. 5 Optical absorption spectra in the UV–VIS–NIR of RM and SWN-RM

(15,030 cm^{-1}), Fig. 5, is assigned to $6A_{1g}(S) \rightarrow 4T_{1g}(G)$ and $6A_{1g}(S) \rightarrow 4T_{2g}(G)$ transitions [27, 28]. Band component analysis identified the splitting of the band at around 18,700 cm^{-1} into two components, 552 and 520 nm (18,115 and 19,240 cm^{-1}). These bands are a characteristic feature of ferric ion and are attributed to the $6A_{1g}(S) \rightarrow 4E_g,4A_{1g}(G)$ transition. The two weak bands on the UV side of the spectrum at 400 and 313 nm (25,000 and 31,985 cm^{-1}) are determined from the Tanabe-Sugano diagram for the Fe^{3+} ion, and are ascribed to the $6A_{1g}(S) \rightarrow 4T_{2g}(D)$ and $6A_{1g}(S) \rightarrow 4T_{1g}(P)$ transitions [29]. The observed band energies and their assignments are given in Table 2, and are compared with assignments of Fe^{3+} bands of Fe_2O_3 and FeOOH polymorphs reported by Sherman and Waite [10]. Characterisation of RM and SWN-RM bands with standard reference patterns of other iron oxides revealed that the band positions matched closely with hematite. Slight deviations in values are suggested to be due to the complexity of red mud, where it is a mixture of both oxides and oxyhydroxides of iron. The VNIR spectra clearly show that peak maxima are observed at slightly different positions for RM and SWN-RM; however, the spectral patterns are very similar. The similarity of the spectra of red mud before and after seawater neutralisation suggests that there is no influence of seawater neutralisation on structural ferric ion.

Near-infrared spectroscopy

NIR spectroscopy displays electronic spectral features of transition metal ions at higher energies (13,000–7,500 cm^{-1}), and vibration bands of anions and molecules from 7,300 to 4,000 cm^{-1}. In NIR spectroscopy all combinations are allowed, i.e. OH-stretching vibrations in Raman can combine with OH-stretching vibrations in infrared to form a NIR band. Therefore, the NIR spectra can be very complex. A broad band centred at 11,630 cm^{-1} (860 nm) in the UV–VIS spectrum appeared as a strong broad band at ~11,300 cm^{-1} in the near-infrared spectrum, figure not shown, with a splitting of two component bands at 11,770 and 10,940 cm^{-1}. These bands are characteristic of the $6A_{1g}(S) \rightarrow 4T_{1g}(G)$ transition band [10, 24] of Fe^{3+} with octahedral coordination. The NIR spectral profile in the 7,300−6,700 cm^{-1} region, Fig. 6, represents bands due to overtones of OH-stretching

Table 2 Energies and assignments of the bands observed in red mud and a comparison with the assignments of Fe^{3+} bands in the electronic spectra of iron oxides (Fe_2O_3) and oxide hydroxides (FeOOH)

Transition	Observed band positions				Reported band positions [10]	
	Red mud		SWN red mud		Hematite	Goethite
	λ (nm)	v (cm^{-1})	λ (nm)	v (cm^{-1})	v (cm^{-1})	v (cm^{-1})
$^6A_{1g}(S) \rightarrow {}^4T_{1g}(G)$	860	11,630	876	11,420	11,300	10,900
$^6A_{1g}(S) \rightarrow {}^4T_{2g}(G)$	665	15,030	664	15,060	15,400	15,400
$^6A_{1g}(S) \rightarrow {}^4E_g,{}^4A_{1g}(G)$	552	18,115	554	18,055	22,500	~23,000
	520	19,240	522	19,170		
$^6A_{1g}(S) \rightarrow {}^4T_{2g}(D)$	400	25,000	401	24,910	24,700	nd
$^6A_{1g}(S) \rightarrow {}^4E_g(D)$	nd	nd	nd	nd	26,300	27,400
$^6A_{1g}(S) \rightarrow {}^4T_{1g}(P)$	313	31,985	310	32,270	31,300	35,000

nd not detected

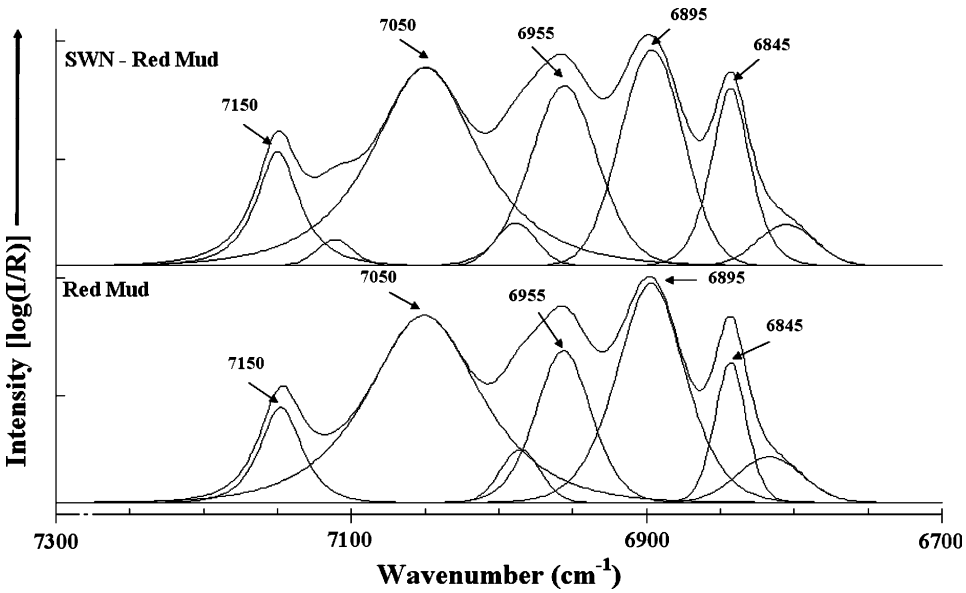

Fig. 6 NIR spectra of RM and SWN-RM of the fundamental overtones of OH-stretching modes

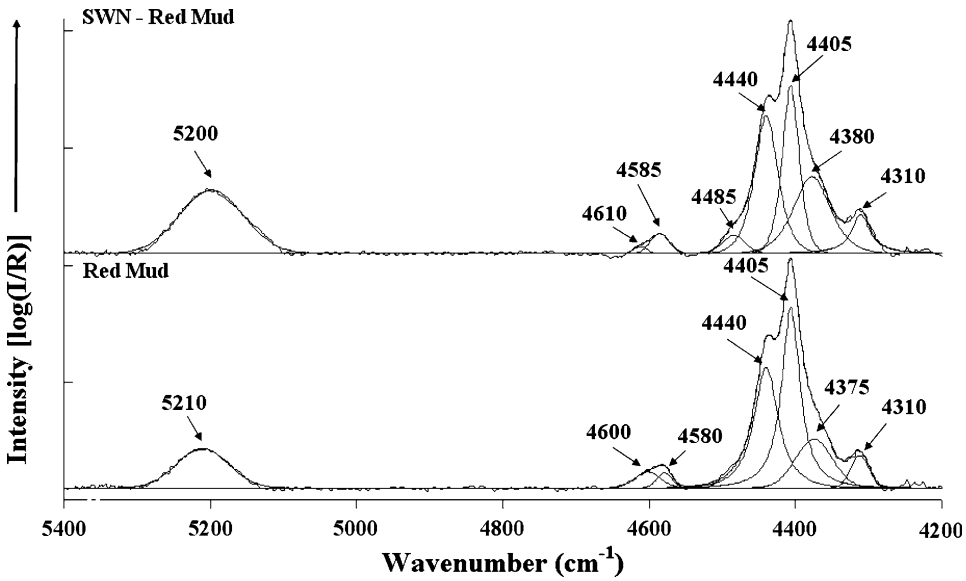

Fig. 7 NIR spectra of RM and SWN-RM in the OH-stretching and deformation vibrational region

fundamental modes. The band centred at 7,050 cm^{-1} with a shoulder band at 7,150 cm^{-1} is attributed to FeOH and AlFeOH groups of oxyhydroxides of iron and aluminium related minerals in red mud. The structural band located at 6,895 cm^{-1} observed with components on either side at 6,955 and 6,845 cm^{-1} are assigned to the overtones of OH-stretching fundamental modes of (SiSi)O–OH, believed to be attributed to cancrinite. Bands at around 6,975 and 6,815 cm^{-1} are believed to be combination bands of the first overtone OH fundamentals of various components of bauxite residues.

The combination bands of the hydroxyl-stretching and deformation vibrations observed in the 5,400–4,200 cm^{-1} region are shown in Fig. 7. One weak band observed at 5,210 cm^{-1} indicates molecular H_2O adsorbed on red mud. The strongest band observed in the spectrum is at 4,405 cm^{-1} with shoulders at 4,440 and 4,375 cm^{-1}, attributed to combination and overtone modes of carbonate (CO_3^{2-}) fundamentals. The observation of the overtones of carbonate ion is in harmony with natural and synthetic aurichalcites that include a series of five bands around 5,200, 5,000, 4,800, 4,400, and 4,200 cm^{-1} [30]. The band near 4,600 cm^{-1} is assigned to Al–OH, and appears weak due to overlapping of carbonate bands in the same region. A low intensity peak at 4,310 cm^{-1} is due to Fe–OH vibrations.

Conclusions

The characterisation of red mud and seawater neutralised red mud proved difficult due to complex band profiles with multiple overlapping bands. However, major constituents of red mud could be identified. XRD identified 12 different mineralogical phases present in red mud and 13 mineralogical phases in SWN red mud. The additional phase in SWN red mud is due to the formation of hydrotalcite during the seawater neutralisation process. The majority of the peaks identified in the Raman spectra were ascribed to hematite, which makes up to 60 wt% of bauxite refinery residues. However, in the infrared spectra hematite was not clearly identified. The complex band profile of the hydroxyl-stretching vibrational region of the infrared spectra was determined to be attributed to gibbsite and boehmite, which are also major mineralogical phases present in red mud. Both XRD and IR techniques observed a decrease in the quantity of gibbsite after seawater neutralisation, and it is believed a phase transition is responsible for this observation. Due to the abundance of carbonate compounds in red mud, multiple bands were observed in the carbonate vibrational region. Bands assigned to whewellite increased in intensity after seawater neutralisation due to the complexation of Ca^{2+} in seawater with oxalic acid in the red mud slurry. IR and Raman identified different mineralogical phases of red mud; therefore, a combination of these techniques is required to study bauxite refinery residues. The observation of two broad bands in RM and SWN-RM near 860 and 400 nm (11,300 and 25,000 cm^{-1}) and a pair of sharp bands centred at 500 nm (20,000 cm^{-1}) are characteristic features of the Fe^{3+}. The observation of identical spectral patterns (both electronic and vibrational spectra) of red mud before and after seawater neutralisation confirmed that there is no effect of seawater neutralisation on structural cationic substitutions such as Al^{3+}, Fe^{3+}, Fe^{2+}, Ti^{3+}.

Acknowledgements The financial and infrastructure support of the Queensland Research and Development Centre (QRDC-RioTintoAlcan) and the Queensland University of Technology Inorganic Materials Research Program of the School of Physical and Chemical Sciences is gratefully acknowledged.

References

1. Hind AR, Bhargava SK, Grocott SC (1999) Colloids Surf A 146:359
2. Jamialahmadi M, Muller-Steinhagen H (1998) JOM 50:44
3. Chvedov D, Ostap S, Le T (2001) Colloids Surf A 182:131
4. Menzies NW, Fulton IM, Morrell WJ (2004) J Environ Qual 33:1877
5. Glenister DJ, Thornberg MR (1985) Chemica 85:100
6. Diaz B, Joiret S, Keddam M, Novoa XR, Perez MC, Takenouti H (2004) Electrochem Methods Corros Res 49:3039
7. Santona L, Castaldi P, Melis P (2006) J Hazard Mater 136:324
8. Hanahan C, McConchie D, Pohl J, Creelman R, Clark M, Stocksiek C (2004) Environ Eng Sci 21:125
9. McConchie D, Clark M, Hanahan C, Davies-McConchie F (2000) In: Proc 3rd Queensland environmental conference, Brisbane, Queensland, Australia, 2000, p 201
10. Sherman DM, Waite TD (1985) Am Mineral 70:1262
11. Palmer SJ, Frost RL, Godwin A, Nguyen T (2008) J Raman Spectrosc 39:395
12. Kloprogge JT, Wharton D, Hickey L, Frost RL (2002) Am Mineral 87:623
13. Castaldi P, Silvetti M, Santone L, Enzo S, Melis P (2008) Clays Clay Miner 56:461
14. Porto SPS, Krishnan RS (1967) J Chem Phys 47:1009
15. Hart TR, Adams SB, Tempkin H (1990) Phys Rev 41:7822
16. Murad E (1997) Am Mineral 82:203
17. Downs RT (2006) 'The RRUFF project: an integrated study of the chemistry, crystallography, Raman and infrared spectroscopy of minerals. http://rruff.info./. Accessed 20 Nov 2006
18. Hermeler G, Buhl JC, Hoffmann W (1991) Catal Today 8:415
19. Farmer VC (1974) The Infrared spectra of minerals. Mineralogical Society, London
20. Frost RL, Kloprogge JT, Russell SC, Szetu J (1999) Appl Spectrosc 53:423
21. Marel HW, Beutelspacher H (1976) Atlas of infrared spectroscopy of clay minerals and their admixtures. Elsevier Scientific Pub. Co, New York
22. Rochester CH, Topham SA (1979) J Chem Soc Faraday Trans 75:1073
23. Gadsden JA (1975) Infrared spectra of minerals and related inorganic compounds. Butterworths, London
24. Hunt GR, Ashley RP (1979) Econ Geol 74:1613
25. Townsend TE (1987) J Geophys Res 92:1441
26. Marfunin A (1979) Physics of minerals and inorganic materials: an introduction. Springer-Verlag, New York
27. Rossman GR (1975) Am Mineral 60:698
28. Rossman GR (1976) Am Mineral 61:398
29. Tanabe Y, Sugano S (1954) J Phys Soc Jpn 9:753
30. Reddy BJ, Frost RL (2007) J Near Infrared Spectrosc 15:115